

Nanomedicine (Lond). Author manuscript; available in PMC 2014 September 19.

Published in final edited form as:

Nanomedicine (Lond). 2014 February; 9(2): 221–235. doi:10.2217/nnm.13.100.

# Biodistribution and clearance of a filamentous plant virus in healthy and tumor-bearing mice

#### Sourabh Shukla,

Department of Biomedical Engineering, Case Western Reserve University, 10900 Euclid Avenue, Cleveland, OH 44106, USA

#### Amy M Wen,

Department of Biomedical Engineering, Case Western Reserve University, 10900 Euclid Avenue, Cleveland, OH 44106, USA

## Nadia R Ayat,

Department of Biomedical Engineering, Case Western Reserve University, 10900 Euclid Avenue, Cleveland, OH 44106, USA

#### Ulrich Commandeur,

Institute for Molecular Biotechnology, RWTH Aachen University, Worringer Weg 1, 52074 Aachen, Germany

#### Ramamurthy Gopalkrishnan,

Department of Biomedical Engineering, Case Western Reserve University, 10900 Euclid Avenue, Cleveland, OH 44106, USA

## Ann-Marie Broome,

Department of Biomedical Engineering, Case Western Reserve University, 10900 Euclid Avenue, Cleveland, OH 44106, USA

## Kristen W Lozada,

Department of Pharmacology, Case Western Reserve University, 10900 Euclid Avenue, Cleveland, OH 44106, USA

## Ruth A Keri, and

© 2013 Future Medicine Ltd

Current address: Ĉenter for Biomedical Imaging, Department of Radiology & Radiological Sciences, Medical University of South Carolina, 68 President Street, Charleston, SC 29425, USA

#### Ethical conduct of research

The authors state that they have obtained appropriate institutional review board approval or have followed the principles outlined in the Declaration of Helsinki for all human or animal experimental investigations. In addition, for investigations involving human subjects, informed consent has been obtained from the participants involved.

#### Financial & competing interests disclosure

This work was supported by grants from the NIH/NIBIB (P30 EB011317 to NF Steinmetz, T32 EB007509 to AM Wen and K01 EB006910-01A1 to A-M Broome), NIH/NCI (Case Comprehensive Cancer Center Pilot Grant P30 CA043703 to NF Steinmetz and RA Keri), Mount Sinai Foundation (to NF Steinmetz), CWRU Start-up Funds (to NF Steinmetz), and Ohio Cancer Research Associates (to NF Steinmetz). The authors have no other relevant affiliations or financial involvement with any organization or entity with a financial interest in or financial conflict with the subject matter or materials discussed in the manuscript apart from those disclosed.

R Twyman (www.writescience.com) is thanked for editing the manuscript. This was supported by the CWRU Start-up Funds to NF Steinmetz.

<sup>\*</sup>Author for correspondence: nicole.steinmetz@case.edu.

Department of Pharmacology, Case Western Reserve University, 10900 Euclid Avenue, Cleveland, OH 44106, USA and Department of Genetics, Case Western Reserve University, 10900 Euclid Avenue, Cleveland, OH 44106, USA and Division of General Medical Sciences-Oncology, Case Western Reserve University, 10900 Euclid Avenue, Cleveland, OH 44106, USA

#### Nicole F Steinmetz\*

Department of Biomedical Engineering, Case Western Reserve University, 10900 Euclid Avenue, Cleveland, OH 44106, USA and Department of Radiology, Case Western Reserve University, 10900 Euclid Avenue, Cleveland, OH 44106, USA and Department of Materials Science & Engineering, Case Western Reserve University, 10900 Euclid Avenue, Cleveland, OH 44106, USA

## **Abstract**

**Aim**—Nanoparticles based on plant viruses are emerging biomaterials for medical applications such as drug delivery and imaging. Their regular structures can undergo genetic and chemical modifications to carry large payloads of cargos, as well as targeting ligands. Of several such platforms under development, only few have been characterized *in vivo*. We recently introduced the filamentous plant virus, potato virus X (PVX), as a new platform. PVX presents with a unique nanoarchitecture and is difficult to synthesize chemically.

**Methods**—Here, we present a detailed analysis of PVX biodistribution and clearance in healthy mice and mouse tumor xenograft models using a combination of *ex vivo* whole-organ imaging, quantitative fluorescence assays and immunofluorescence microscopy.

**Results & conclusion**—While up to 30% of the PVX signal was from the colon, mammary and brain tumor tissues, remaining particles were cleared by the reticuloendothelial system organs (the spleen and liver), followed by slower processing and clearance through the kidneys and bile.

#### **Keywords**

anisotropic nanoparticle; biodistribution; immunogenicity; mononuclear phagocyte system; nanoparticle shape; polyethylene glycol; tumor homing; viral nanoparticle

Plant viruses and bacteriophages have been recognized as potentially useful biomaterials for a range of nanomedical applications, including tissue-specific imaging, drug delivery and vaccine development [1]. Viruses are versatile because they are symmetrical, monodisperse protein structures that form icosahedrons, tubes or filaments, which encapsulate nucleic acids and deliver them efficiently to cells. They have evolved robust structures that withstand the adverse conditions present during infection, but remain responsive to subtle physiological parameters, such as pH and temperature, allowing them to disassemble and reassemble for self-propagation. These attributes can be exploited to develop virus-based nanoparticles (VNPs) that are amenable to chemical and genetic modification, allowing the incorporation of drugs, contrast and imaging probes, as well as targeting ligands conjugated to either the external or internal particle surface, or packaged inside through the use of induced disassembly and reassembly strategies [2]. The ease of production by molecular farming in plants makes VNP technology highly scalable.

The application and development of plant VNPs is still a relatively young discipline. Although various platforms have been tested and developed in the test tube (e.g., various modification strategies have been devised), only few examples have been characterized *in vivo*; principally, the icosahedrons cowpea chlorotic mottle virus (CCMV) and cowpea mosaic virus (CPMV) [3,4]. Both plant VNPs demonstrated rapid blood pool clearance and were detected in a wide variety of tissues throughout the body; CPMV accumulated primarily in the liver and spleen, whereas CCMV particles were mostly found in the thyroid gland (but also in the liver, spleen, bladder and salivary glands). Pathology or toxicity was not reported, despite the broad biodistribution.

CCMV and CPMV are both 30-nm-sized icosahedrons with T = 3 symmetry; and the majority of medical research using VNPs has focused on the application of VNPs with icosahedral symmetry. However, recent data from nanomedical engineering research have indicated that nonspherical, elongated materials may be preferred for the development of cargo-delivery vehicles; data indicate that nonspherical and high aspect ratio materials are more likely to evade internalization by macrophages, resulting in prolonged circulation followed by enhanced tumor deposition [5]. Furthermore, nonspherical shapes have enhanced margination properties and, hence, a higher likelihood for deposition in tumor tissue [6–8].

Therefore, we recently turned toward the development of the filamentous plant virus, potato virus X (PVX), as a vehicle for cargo delivery to tumor cells and tissues. PVX measures 515  $\times$  13 nm, with a flexible filamentous structure, which is difficult to replicate using synthetic chemistry. In a recent study, we demonstrated that PVX and CPMV have distinct *in vivo* profiles with CPMV homing predominantly to the liver and, to a lesser extent, the spleen, whereas PVX was predominantly taken up by the spleen and, to a lesser extent, the liver [9]. Significant differences were observed with regard to tumor homing: PVX showed enhanced tumor homing, especially in the core of the tumor xenografts (fibrosarcoma, squamous sarcoma and colon cancer) in both avian and mouse tumor models [9].

The enhanced tumor-homing properties of PVX, combined with its large surface area offering a higher loading capacity for cargos, renders PVX an attractive platform for the development of novel nanomedical formulations. In this work, we describe PVX biodistribution and clearance in healthy mice and mouse models of colon, breast and brain cancer. A combination of *ex vivo* whole-organ imaging, quantitative fluorescence assays on homogenized tissues and immunofluorescence microscopy provides detailed analysis of the *in vivo* fate of PVX over a 5-day time course. The data gained provide fundamental information of the *in vivo* behavior of PVX, essential for further tailoring and development of the platform for potential clinical applications.

## **Methods**

## **PVX** propagation

PVX was propagated in *Nicotiana benthamiana*. Leaves were harvested 10–14 days after mechanical inoculation with 5 µg of purified PVX particles. PVX was purified as described

earlier (please see Supplementary Material online at www.futuremedicine.com/doi/suppl/ 13.75) [9].

## Bioconjugate chemistry to modify PVX with A647 & polyethylene glycol

Purified PVX was prepared at a concentration of 2 mg/ml in 0.1 M potassium phosphate buffer (pH 7.0) and was incubated with NHS-PEG5000 (NANOCS, NY, USA) and NHS-A647 (Life Technologies, NY, USA) using a one-pot synthesis protocol (Figure 1A). The reagents were added to a 10% (volume/volume) final concentration in DMSO and incubated overnight at room temperature, with agitation. Polyethylene glycol (PEG) and A647 were added at a molar excess of 4000 and 2500, respectively (PVX has a molar mass of  $3.5 \times 10^7$  g/mol). VNP formulations were purified by dialysis and 10-kDa cut-off centrifugal filtration (Millipore, MA, USA).

## **UV/visible spectroscopy**

Labeling efficiency with fluorophores was determined by UV/visible spectroscopy using a NanoDrop® (Thermo Scientific, DE, USA) instrument. The number of A647 labels per virion was calculated based on the Beer–Lambert law using the specific extinction coefficients for PVX ( $2.97~\text{ml}^{-1}\text{mg}^{-1}\text{cm}^{-1}$  at 260~nm) and A647 ( $270,000~\text{M}^{-1}\text{cm}^{-1}$  at 650~nm).

## Denaturing gel electrophoresis

Denaturing SDS-PAGE was used to confirm the conjugation of PEG chains to individual coat proteins. We analyzed 10  $\mu$ g of denatured protein samples on 4–12% NuPage<sup>®</sup> gels (Life Technologies) in 1× 3-morpholinopropane-1-sulfonic acid SDS running buffer (Life Technologies). Protein bands were visualized under white light after staining with Coomassie Brilliant Blue (Fisher BioReagents, PA, USA; 0.25% weight/volume).

#### Transmission electron microscopy

Diluted samples of A647-PVX-PEG5000 nanoparticles (20  $\mu$ l; 0.1 mg/ml) were negatively stained with 2% (weight/volume) uranyl acetate for 2 min on a carbon-coated copper grid. Samples were analyzed using a Zeiss Libra® 200FE (Carl Zeiss Microscopy, NY, USA) transmission electron microscope at 200 kV.

## **PVX** biodistribution

All animal studies were carried out using Institutional Animal Care and Use Committee-approved procedures. The biodistribution of A647-PVX-PEG particles in BALB/c mice was profiled by *ex vivo* fluorescence imaging of intact tissues using the Maestro<sup>™</sup> Imaging System (Perkin Elmer, MA, USA), or quantitative fluorescence detection in tissue homogenates using a Tecan Infinite<sup>®</sup> M200 fluorescence plate reader (Tecan Systems Inc., CA, USA; Supplementary Material).

#### Tumor homing & imaging using mouse xenograft models

Tumor homing was investigated using subcutaneous tumor xenograft models of human colon (HT-29) and brain cancer (Gli36D5) in NCr *nu/nu* nude mice, and orthotopic 4T1 mammary tumor xenografts in 8-week-old female BALB/c mice (Supplementary Material).

#### Immunofluorescence & confocal & fluorescence microscopy

We prepared 10-µm cryosections from frozen isolated organs using a Leica CM 1850 (Leica Microsystems Inc., IL, USA) cryomicrotome. After fixation, frozen tissue sections were stained for different markers, including CD31 (endothelial cells), F4/80 (macrophages), CD3 (T cells), CD45R/B220 (B-cell follicles) and LAG-3/CD223 (activated T cells) using combinations of primary and secondary antibodies (Supplementary Material). Slides were analyzed using a Zeiss Axio<sup>®</sup> Observer Z1 (Carl Zeiss Microscopy) motorized FL inverted microscope and by confocal microscopy using a Fluoview FV1000 (Olympus America, PA, USA).

#### **Results & discussion**

## **Production of PVX**

PVX filaments were isolated from infected *Nicotiana benthamiana* plants, yielding 0.5–1.0 mg of pure PVX per gram of infected leaves. The concentration of PVX in plant extracts was determined by UV/visible spectroscopy using the PVX extinction coefficient of 2.97 mg<sup>-1</sup>ml<sup>-1</sup>cm<sup>-1</sup>. The purity of the PVX preparation was confirmed based on the A260:A280 ratio of 1.2, indicating pure and intact PVX filaments. The structural integrity of the purified VNPs was also confirmed by transmission electron microscopy analysis (data not shown).

## Chemical modification of PVX with PEG5000 & A647

PVX has an aspect ratio of 40, reflecting its filamentous structure ( $515 \times 13$  nm). Each filament comprises 1270 identical copies of a single 25-kDa coat protein. Bioconjugation using N-hydroxysuccinimide active esters targeting solvent-exposed lysine side chains allows the functionalization of each coat protein. We conjugated PVX with the near-infrared fluorophore A647 to allow the imaging and tracking of the formulations, and also with PEG to enhance particle solubility and stability. A647 and PEG5000 were chosen because we recently showed that A647-PVX-PEG is suitable for tumor homing and imaging in preclinical tumor animal models [9]. We therefore designed the PVX formulation according to our published procedures (Figure 1A) [9]. Transmission electron microscopy imaging confirmed that the particles maintained their structural integrity and filamentous shape after modification (Figure 1B). The appearance of higher-molecular-weight protein bands following denaturing SDS-PAGE indicated covalent attachment of PEG5000 chains to PVX as anticipated (Figure 1C). The multiple bands suggested that PEGylation may prevent the complete denaturation of PVX capsids into single-copy coat proteins (i.e., the highermolecular-weight bands are likely to be dimers of PEGylated coat proteins). We measured the intensity of the bands using ImageJ (NIH, MD, USA) software to determine the degree of PEGylation, and found that approximately 30% of the coat proteins were modified with PEG, equivalent to approximately 380 PEG5000 chains per PVX particle. UV/visible spectroscopy was used to determine the number of dye labels per PVX particle using the

corresponding extinction coefficients and the Beer–Lambert law. We found that the density of A647 was similar to PEG5000 (i.e., 380 A647 labels per PVX; Figure 1D). The chemical conjugation was highly reproducible, with only 10% batch-to-batch variation. This density of A647 labeling yields intensely fluorescent PVX nanofilaments, which do not undergo fluorescence quenching (data not shown). The zeta potential of the particles suspended in phosphate-buffered saline (PBS) buffer (pH 7.0) was measured to be  $24.9 \pm 8.2$  mV [9].

#### **Biodistribution of PVX**

Several methods are available to study the biodistribution of nanoparticles and their cargos, including HPLC [10], inductively coupled plasma atomic emission spectroscopy/mass spectroscopy [4], radiolabeling followed by scintillation counting [11], PET [12] and fluorescence-based assays [13,14]. The latter approach has gained popularity because it is rapid and inexpensive. Nanomaterials can also be labeled with near-infrared dyes suitable for live imaging, *ex vivo* whole-organ imaging and the quantitative analysis of fluorescence in tissue homogenates [13,15].

We studied the biodistribution of A647-PVX-PEG using a combination of quantitative platereader assays and *ex vivo* imaging of whole organs. For the quantitative assays, A647-PVX-PEG was administered at 10 mg/kg bodyweight into the tail veins of BALB/c mice, and the brain, lungs, heart, kidneys, liver and spleen were removed and homogenized at time intervals of 2, 6, 24 and 48 h (n = 4 per time point). The fluorescence signals were normalized against tissues from animals injected with PBS and the fluorescence intensity per gram of tissue weight was determined (Figure 2A). For the whole-organ assays, A647-PVX-PEG was administered as described above and organs were removed for imaging using the Maestro Imaging System, 24 and 72 h after injection (n = 3 per time point; Figure 2B).

As evident from the fluorescence data, there is some degree of variability between animals, especially at the early time points (i.e., 2 vs 6 h postadministration). Overall, the trend indicates PVX was cleared from the circulation and accumulated in the spleen > liver > kidneys within 2–6 h postadministration (Figure 2A). Similarly, high variations between animals were previously reported studying the CPMV nanoparticle platform [9]. For future studies (e.g., evaluation of different cargo-loaded or targeted PVX formulations), it will be necessary to increase the number of animals per group to yield statistically significant data. In the present study, however, we focused our studies on the evaluation of only one PVX-based formulation modified with dyes and PEG; this formulation could be regarded as a universal platform for future cargo loading and delivery. In all four animals studied, the trend was the same, indicating sequestration of PVX within 2–6 h in the mononuclear phagocyte system (MPS) of the spleen and liver (Figure 2A), consistent with the short half-life of A647-PVX-PEG of 12.5 min [9].

At longer time points (i.e., 24–48 h), signals fade, indicating clearance from the body. The presence of fluorescence signals in the kidneys may also indicate renal clearance. Strong fluorescence signals in the stools of the animals also suggest processing and clearance through the hepatobiliary system (data not shown). We noted weak signals from the lungs, consistent with previous reports on other elongated nanoparticles [16,17].

The plate-reader assays showed that fluorescence signals could no longer be detected in tissues isolated 48 h postadministration. Faded fluorescence signals could still be detected using the Maestro Imaging System *ex vivo* imaging at longer time points (72 h; Figure 2B), indicating it may take several days for clearance of PVX from tissues (this is similar to observations made studying the *in vivo* fate of CPMV [9]). A more sensitive assay may be required to determine the timing of clearance more accurately.

The *in vivo* fate of nanoparticles is governed by their physiological properties such as size, shape, composition, surface chemistry and physical properties [18,19]. The biodistribution profile observed for PVX matches previous reports for nanomaterials of similar size, shape and composition. Spherical nanomaterials 30–80 nm in diameter tend to be sequestered in the lungs and leaky vasculature, whereas those larger than 80 nm are generally trapped in the spleen and liver [20,21]. Nanomaterials similar in size to PVX are not usually excreted by the renal system, but are mainly removed from circulation efficiently by the MPS [18,19,22].

The MPS versus renal clearance has been studied using carbon nanotubes, a synthetic class of high aspect ratio nanomaterials. Data remain elusive; while pristine single-walled carbon nanotubes (SWCNTs) showed significant accumulation in the liver only [23], PEGylated SWCNTs were found in the liver and spleen [16]. Some functionalized SWCNTs and multiwalled carbon nanotubes on the other hand, showed efficient renal clearance [24–26]. Modeling indicated that surface chemistry may impact the orientation of the nanotubes towards the glomerula capillary pores, thus promoting renal clearance despite the high molecular weight [27].

Our data indicate that PVX is cleared mainly by MPS (vs renal filtration); however, a combination of clearance mechanisms may play a role. Based on the small dimensions along the short axis, renal clearance of PVX cannot be ruled out. Alternatively, it is also possible that digested or broken PVX fragments are routed through the kidneys. Nevertheless, it is indicated that the majority of the injected dose underwent hepatobiliary processing followed by excretion into the bile and feces. This is consistent with the behavior of elongated mesoporous silica nanoparticles and SWCNTs [28,29]. These hard, inorganic materials are secreted into the bile slowly (e.g., it took 2 months for SWCNTs to be cleared from mice by hepatobiliary and renal processing) [16]. By contrast, we found that PVX was cleared within a few days (Figure 2).

#### Liver & spleen immunofluorescence following the administration PVX

Nanoparticles tend to be sequestered rapidly by dendritic cells, blood monocytes and tissue-resident macrophages in the liver, spleen and lymph nodes, which are responsible for clearing, processing and degrading foreign materials from circulation [30–32]. We evaluated the association of PVX with resident macrophages in the liver and spleen by preparing cryosections of these tissues from mice injected with A647-PVX-PEG or with PBS as a control, and staining them with 4',6-diamidino-2-phenylindole and antibodies for the detection of CD31 (endothelial cells) and F4/80, which is expressed in a range of macrophages, irrespective of lineage [33]. Confocal microscopy was used to colocalize PVX (labeled directly with A647) and macrophages stained with anti-F4/80 (detected with a

secondary antibody conjugated to A555). Strong PVX signals (green) were detected in the liver and spleen at 24 and 72 h postinjection, and these were colocalized with the magenta signals from F4/80-stained macrophages in the liver (Figure 3A & 3B), whereas in the spleen the signals remained separate (Figure 3C & 3D). Mander's colocalization coefficients (M2 values) were determined using ImageJ resulting in values of 0.351 and 0.913 for the liver at 24 and 72 h, respectively (Table 1), probably reflecting the uptake of PVX by Kupffer cells [33]. Colocalization with endothelial cells stained with an antibody against CD31 showed the opposite trend, with M2 values falling from 0.976 to 0.379 between 24 and 72 h (Table 1 & Supplementary Figure 1). In the spleen, PVX did not colocalize significantly with either CD31 or F4/80 (Table 1). The relative positions of F4/80 and PVX staining in the spleen indicate that PVX filaments are sequestered into the white pulp, surrounded by the red pulp, which comprises F4/80-positive macrophages (Figure 3C & 3D).

The spleen is a secondary lymphoid organ with a central role in primary defense against all types of antigens that appear in the circulation, and it is a major site of antibody production [34]. Nanoparticles may be taken up by a variety of immune cells in the bloodstream and in tissues. To gain further insight into the tissue distribution of PVX within the spleen, composite images of entire spleens were generated using a Zeiss Axio Observer Z1 FL inverted microscope fitted with a motorized stage (Figure 4). It was found that PVX filaments were clustered, and accumulated in the white pulp regions of the spleen (Figure 4). We used fluorescence and confocal imaging to study the colocalization of PVX with B-cell follicles using B220 as a marker (Figure 4A & 4B) [35,36], T cells using CD3 as a marker (Figure 4C & 4D) [37] and activated T cells using CD223 as a marker (Figure 4E & 4F) [38]. A647-PVX-PEG appeared to colocalize with B220<sup>+</sup> B cells in the white pulp (Figure 4A & 4B) supported by M2 values of 0.866 and 0.762 at 24 and 72 h postinjection, respectively (Table 1). Although there was no apparent colocalization with CD223 or CD3, there was a significant increase in CD223<sup>+</sup> cells 72 h postinjection compared with the 24-h time point (Figure 4C & 4D).

The accumulation of PVX filaments in B cells combined with the higher number of T cells in the spleen may indicate that PVX particles are immunogenic. The sequestration of PVX into B220<sup>+</sup> B cells indicates the induction of a humoral immune response (reflecting the transport of antigens to B-cell follicles for germinal center reactions and affinity maturation) [39], whereas the recruitment and activation of CD223<sup>+</sup> T cells may also indicate the induction of a cellular immune response [40]. This may imply that decoration of PVX with 380 PEG5000 chains is insufficient to achieve effective shielding from uptake in antigenpresenting cells. This is an important observation because the development of VNPs thus far has focused on the use of low-molecular-weight PEG chains, such as PEG500 [41], PEG1000 and PEG2000 [42]. Further research is therefore required to determine exactly how VNPs based on plant viruses interact with the immune system and whether shielding chemistries, such as PEGylation, are sufficient to prevent immunogenicity (see 'Conclusion' section).

#### PVX-tumor-homing studies in preclinical mouse models

We have previously demonstrated that elongated PVX filaments achieve strong tumor homing and accumulation in a mouse tumor model of colon cancer and a chicken chorioallantoic membrane model of squamous carcinoma and fibrosarcoma [9]. This may be consistent with the tumor-homing properties of other filamentous nanoparticles (e.g., filomicelles) [22,43,44]. Here, we investigated PVX–tumor homing in a set of mouse tumor models representing colon, brain and breast cancer.

Time-course studies were conducted over a 5-day time frame using a HT-29 (colon cancer) NCr *nu/nu* mouse tumor xenograft model. A single dose of A647-PVX-PEG (10 mg/kg bodyweight) was injected into the tail vein (n = 3) and tissues were collected for analysis using the Maestro Imaging System *ex vivo* imaging, immunofluorescence staining and confocal microscopy after 5, 24, 72 and 120 h (Figure 5). Tumor homing was not evident after 5 h, but strong fluorescence signals were observed at the 24-h time point, indicating the strong homing of PVX to HT-29 tumors. At 24–72 h, PVX–tumor accumulation accounted for 30% of the detected signal; the remaining particles appeared sequestered in the liver and spleen, reflecting MPS clearance (as discussed above). Fluorescence in the tumor and in the liver dropped significantly after 5 days as the PVX particles were cleared. Strong signals from the kidneys indicated the degradation of PVX followed by renal filtration en route to the bladder (Figure 5B). This is also consistent with findings from healthy BALB/c mice where clearance through the bile and urine is indicated.

Particularly interesting is the fact that the observed fluorescence from the tumors at 5 h is significantly lower compared with the liver and spleen. At later time points, 24–72 h postadministration, tumor homing increases significantly and accounted for 30% of the detected signal. This is interesting because PVX has a plasma circulation half-life of only 12.5 min. Tumor homing solely based on enhanced permeability and retention effects is thus unlikely. Data indicate that another mechanism plays a role in tumor homing and transport. The potential exists that tumor accumulation could be mediated by the phagocytosis of PVX followed by migration of the phagocytes into tumors. Similar mechanisms have been proposed for inorganic nanoparticles [45]. Immunofluorescence data indicate that PVX filaments accumulated close to the endothelium (stained with an antibody specific for CD31), but were not colocalized or confined within the endothelium (Figure 5A). We have stained tumor sections for macrophage markers, but could not find evidence of colocalization of PVX with the markers studied (Supplementary Figure 2). Future studies must be carried out to elucidate the tumor-homing mechanism of PVX and to identify its intratumoral localization. Others have reported that transport of nanoparticles between the blood and organs could be reversible [46]; if this holds true for PVX, this could also explain delayed accumulation of PVX in tumors.

We also tested the tumor-homing characteristics of PVX using two other preclinical mouse models, an ectopic Gli36 5 brain tumor xenograft in NCr *nu/nu* mice and an orthotopic 4T1 mammary tumor xenograft in the mammalian glands of female BALB/c mice. A647-PVX-PEG was injected into the tail vein of both models, and tumors were harvested along with other tissues from sacrificed mice after 24 h. The Maestro Imaging System confirmed tumor

homing in both the 4T1 and Gli36 5 xenografts, which showed significantly higher fluorescence signal intensities compared with tumors from control mice injected with PBS (Figure 5C).

PVX-tumor homing was observed in all three tumor models, but the fluorescence signals compared with the PBS controls were generally stronger in the HT-29 model than the others (Figure 5C). The uptake of VNPs by the tumor depends on many physiological parameters, including vascular and collagen density, which affect interstitial pressure and, hence, extravasation [47]. Furthermore, secondary mechanisms of PVX-tumor homing must be considered; parameters influencing tumor accumulation could be related to the degree of macrophage infiltration and other immune-regulatory characteristics. CD31 staining suggested that HT29 and 4T1 tumors were more vascularized than Gli36 5 tumors (Figure 6). Furthermore, based on the colocalization coefficients (Table 1), PVX appears to be relatively more associated with the vasculature (CD31) in Gli36 5 tumors than the other models. This could also indicate that PVX extravasates less efficiently from the Gli36 5 tumor vasculature into the tumor, and thus accumulates to a lower level. Sections from each tumor were stained for B-cell markers (B220) and macrophage markers (F4/80) in order to observe any association of PVX with these cell types within the tumor microenvironment (Supplementary Figure 2). However, we did not observe any significant colocalization of PVX with either of the cell populations within the tumors.

## Conclusion

In conclusion, biodistribution and the physiological fate of PVX-based nanoparticles are described; a set of healthy mice and mouse models of human tumors were studied over a 5-day time course. Biodistribution and clearance studies suggest that PVX is sequestered in MPS organs, the spleen and liver; clearance occurs after several days through the hepatobiliary system and, to a smaller degree, via renal clearance.

In the liver, PVX colocalizes with F4/80-positive macrophages, likely to be Kupffer cells [33]. In the spleen, PVX filaments were localized within the white pulp, specifically B-cell follicles. The accumulation of PVX within B cells indicates that the formulation evaluated shows intrinsic immunogenicity. Besides all the advantages of VNPs, such as ease of production, reproducible genetic and chemical modification, monodisperse structures, various shapes and sizes (which are naturally available), and stability under various bathing conditions, a potential hurdle toward clinical translation of these protein-based carrier systems is that the repetitive coat proteins can induce an immune response and, thus, hamper biocompatibility [48].

It has been generally accepted that PEGylation is a reliable strategy to overcome immunogenicity [49,50]; nevertheless, the effectiveness of the 'stealth' effect and avoidance of immune surveillance must be carefully evaluated. Variables to test are the PEGylation density, confirmation and attachment sites. Research on VNPs has focused on the application of low-molecular-weight PEG chains such as PEG500 [41], PEG1000 and PEG2000 [42]. We report here the application of PEG5000.

The PEG conformation (brush vs mushroom) on the nanoparticle surface is a key parameter that influences biodistribution and clearance. Overall, the more PEG chains attached and the more densely packed they are (favoring the brush conformation), the more effectively the formulation is shielded from opsonization and phagocytosis [51]. The PEG conformation depends on the grafting density and Flory radius ( $R_{\rm F} = aN^{3/5}$  where a is the persistence length of the PEG monomer [a = 0.35 nm] [52] and N is the number of PEG monomers). If the grafting density is less than the Flory radius, the PEG chains adopt a mushroom conformation, whereas grafting densities higher than the Flory radius result in an extended brush conformation [53]. Given that approximately 380 PEG chains are attached to our PVX particles, taking into account their surface area of the 515 nm × 13 nm cylinder, we calculated that one PEG5000 chain is attached to every 56 nm along the filament on average. The Flory dimension of PEG5000 is approximately 6 nm, which suggests the PEG chains adopt a mushroom conformation on the PVX surface. To achieve PEGylation with PEG chains being presented in the brush confirmation, labeling efficiency must be significantly increased; for example, a conjugation of approximately 600 PEG chains with a molecular weight of 20,000 Da, may cause a transition to the brush conformation.

Profound tumor homing with titers reaching up to 30% of the detected PVX signal accumulating in the tumor tissue was observed. A647-PVX-PEG5000, used in this study, has a short plasma circulation time of  $t_{1/2}=12.5\,\mathrm{min}$  [9]. It was therefore interesting to observe that tumor homing significantly increases after 24–72 h postadministration compared with the 5-h time point. Clearance from the blood pool within minutes is thus not consistent with tumor homing via the enhanced permeability and retention effect. We hypothesize that other mechanisms lead to the delayed tumor accumulation of PVX. It is possible that circulating mononuclear phagocytotic cells or other blood components take up PVX and transport the nanoparticles to the tumor tissue. Immunofluorescence data indicate localization of PVX in near proximity of the endothelium; however, the intratumoral localization of PVX is yet to be identified. Mechanistic studies must be carried out to identify the cell types PVX associates with; this is important for further tailoring of PVX as a cargo-delivery vehicle.

PVX is potentially an interesting platform for drug delivery and imaging because of its large surface area and corresponding high payload capacity, its biodegradability and its efficient tumor-homing properties. The discipline of plant-based VNP technology in drug delivery is still emerging – only few VNP-based materials have undergone *in vivo* testing. Understanding biodistribution and clearance is the first step towards tailoring a particular VNP platform for potential clinical applications.

# **Future perspective**

With a significantly improved understanding of nanoparticles, clearance mechanisms and biological fates, several novel nanoparticle platforms will be able to make the crucial transition from preclinical to clinical studies. The majority of these platforms will be based on biodegradable materials that will carry payloads of therapeutic molecules and contrast agents for therapeutic or imaging applications. The addition of targeting ligand is expected to partition nanoparticle carriers to target tissues while minimizing accumulation within

nontarget cells, tissues and organs. In addition, with the development of improved surface passivation strategies, such as camouflage with self-peptides or different stealth polymers (e.g., zwitterionic polymers), in conjugation with the evolving shapes, prolonged circulation of nanocarriers will materialize, resulting in availability of sustained dosages of therapeutic molecules and necessity for fewer repetitive administrations. These factors, together, are expected to improve outcomes of nanomaterial-based therapeutic strategies with reduced toxicity and adverse effects.

# **Supplementary Material**

Refer to Web version on PubMed Central for supplementary material.

# Acknowledgments

The authors thank A Levine (Department of Medicine, Case Western Reserve University, OH, USA) for helpful discussions regarding potato virus X biodistribution and biomarker colocalization, and SC Alexander for assistance with the tissue culture.

## References

Papers of special note have been highlighted as:

- of interest
- of considerable interest
- 1=. Yildiz I, Shukla S, Steinmetz NF. Applications of viral nanoparticles in medicine. Curr Opin Biotechnol. 2011; 22(6):901–908. Provides a broad overview of viral nanoparticles and advances in their biomedical applications. [PubMed: 21592772]
- 2 Pokorski JK, Steinmetz NF. The art of engineering viral nanoparticles. Mol Pharm. 2011; 8(1):29–43. Comprehensive review of chemical and genetic engineering methods employed for designing viral nanoparticles for biomedical applications. [PubMed: 21047140]
- Kaiser CR, Flenniken ML, Gillitzer E, et al. Biodistribution studies of protein cage nanoparticles demonstrate broad tissue distribution and rapid clearance in vivo. Int J Nanomed. 2007; 2(4):715– 733.
- 4. Singh P, Prasuhn D, Yeh RM, et al. Biodistribution, toxicity and pathology of cowpea mosaic virus nanoparticles in vivo. J Control Release. 2007; 120(1–2):41–50. Presents a comprehensive data set evaluating the biodistribution, clearance and pathology of icosahedron cowpea mosaic virus in a mouse model. [PubMed: 17512998]
- 5. Decuzzi P, Godin B, Tanaka T, et al. Size and shape effects in the biodistribution of intravascularly injected particles. J Control Release. 2010; 141(3):320–327. Describes the distinct pharmacokinetic properties and differential biological fates of nanoparticles as influenced by their shapes. This work illustrates why some nanoparticle shapes could be advantageous over others for *in vivo* applications. [PubMed: 19874859]
- 6. Decuzzi P, Ferrari M. The adhesive strength of non-spherical particles mediated by specific interactions. Biomaterials. 2006; 27(30):5307–5314. [PubMed: 16797691]
- 7. Gentile F, Chiappini C, Fine D, et al. The effect of shape on the margination dynamics of non-neutrally buoyant particles in two-dimensional shear flows. J Biomech. 2008; 41(10):2312–2318. [PubMed: 18571181]
- 8. Lee SY, Ferrari M, Decuzzi P. Design of biomimetic particles with enhanced vascular interaction. J Biomech. 2009; 42(12):1885–1890. [PubMed: 19523635]
- 9. Shukla S, Ablack AL, Wen AM, Lee KL, Lewis JD, Steinmetz NF. Increased tumor homing and tissue penetration of the filamentous plant viral nanoparticle potato virus X. Mol Pharm. 2013;

- 10(1):33–42. Presents a comparative account of tumor-homing properties of potato virus X and cowpea mosaic virus viral nanoparticles as influenced by their shapes. [PubMed: 22731633]
- Oliveira LT, Garcia GM, Kano EK, Tedesco AC, Mosqueira VC. HPLC-FLD methods to quantify chloroaluminum phthalocyanine in nanoparticles, plasma and tissue: application in pharmacokinetic and biodistribution studies. J Pharm Biomed Anal. 2011; 56(1):70–77. [PubMed: 21596512]
- 11. Ocampo-Garcia BE, de Ramirez FM, Ferro-Flores G, et al. (99m)Tc-labelled gold nanoparticles capped with HYNIC-peptide/mannose for sentinel lymph node detection. Nucl Med Biol. 2011; 38(1):1–11. [PubMed: 21220124]
- Rojas S, Gispert JD, Martin R, et al. Biodistribution of amino-functionalized diamond nanoparticles. *In vivo* studies based on <sup>18</sup>F radionuclide emission. ACS Nano. 2011; 5(7):5552– 5559. [PubMed: 21657210]
- 13. Artzi N, Oliva N, Puron C, et al. *In vivo* and *in vitro* tracking of erosion in biodegradable materials using non-invasive fluorescence imaging. Nat Mater. 2011; 10(9):704–709. [PubMed: 21857678]
- 14. Vasquez KO, Casavant C, Peterson JD. Quantitative whole body biodistribution of fluorescent-labeled agents by non-invasive tomographic imaging. PLoS ONE. 2011; 6(6):e20594. [PubMed: 21731618]
- 15. Rae CS, Khor IW, Wang Q, et al. Systemic trafficking of plant virus nanoparticles in mice via the oral route. Virology. 2005; 343(2):224–235. [PubMed: 16185741]
- Liu Z, Davis C, Cai W, He L, Chen X, Dai H. Circulation and long-term fate of functionalized, biocompatible single-walled carbon nanotubes in mice probed by Raman spectroscopy. Proc Natl Acad Sci USA. 2008; 105(5):1410–1415. [PubMed: 18230737]
- Yu T, Hubbard D, Ray A, Ghandehari H. *In vivo* biodistribution and pharmacokinetics of silica nanoparticles as a function of geometry, porosity and surface characteristics. J Control Release. 2012; 163(1):46–54. [PubMed: 22684119]
- 18. Li SD, Huang L. Pharmacokinetics and biodistribution of nanoparticles. Mol Pharm. 2008; 5(4): 496–504. [PubMed: 18611037]
- 19. Sa LT, Albernaz MD, Patricio BF, et al. Biodistribution of nanoparticles: Initial considerations. J Pharm Biomed Anal. 2012; 70:602–604. [PubMed: 22742922]
- 20. Lunov O, Syrovets T, Loos C, et al. Differential uptake of functionalized polystyrene nanoparticles by human macrophages and a monocytic cell line. ACS Nano. 2011; 5(3):1657–1669. [PubMed: 21344890]
- 21. Maldiney T, Richard C, Seguin J, Wattier N, Bessodes M, Scherman D. Effect of core diameter, surface coating, and PEG chain length on the biodistribution of persistent luminescence nanoparticles in mice. ACS Nano. 2011; 5(2):854–862. Describes the influence of polyethylene glycol density, chain length and conformation on nanoparticle clearance by the reticuloendothelial system, biodistribution and pharmacokinetics. [PubMed: 21291197]
- 22. Bartneck M, Keul HA, Wambach M, et al. Effects of nanoparticle surface-coupled peptides, functional endgroups, and charge on intracellular distribution and functionality of human primary reticuloendothelial cells. Nanomedicine. 2012; 8(8):1282–1292. [PubMed: 22406188]
- Cherukuri P, Gannon CJ, Leeuw TK, et al. Mammalian pharmacokinetics of carbon nanotubes using intrinsic near-infrared fluorescence. Proc Natl Acad Sci USA. 2006; 103(50):18882–18886.
   [PubMed: 17135351]
- 24. Lacerda L, Herrero MA, Venner K, Bianco A, Prato M, Kostarelos K. Carbon-nanotube shape and individualization critical for renal excretion. Small. 2008; 4(8):1130–1132. [PubMed: 18666166]
- 25. Mcdevitt MR, Chattopadhyay D, Kappel BJ, et al. Tumor targeting with antibody-functionalized, radiolabeled carbon nanotubes. J Nucl Med. 2007; 48(7):1180–1189. [PubMed: 17607040]
- Singh R, Pantarotto D, Lacerda L, et al. Tissue biodistribution and blood clearance rates of intravenously administered carbon nanotube radiotracers. Proc Natl Acad Sci USA. 2006; 103(9): 3357–3362. [PubMed: 16492781]
- 27. Ruggiero A, Villa CH, Bander E, et al. Paradoxical glomerular filtration of carbon nanotubes. Proc Natl Acad Sci USA. 2010; 107(27):12369–12374. [PubMed: 20566862]
- 28. Huang X, Li L, Liu T, et al. The shape effect of mesoporous silica nanoparticles on biodistribution, clearance, and biocompatibility *in vivo*. ACS Nano. 2011; 5(7):5390–5399. [PubMed: 21634407]

29. Choi HS, Liu W, Misra P, et al. Renal clearance of quantum dots. Nat Biotechnol. 2007; 25(10): 1165–1170. [PubMed: 17891134]

- 30. Owens DE 3rd, Peppas NA. Opsonization, biodistribution, and pharmacokinetics of polymeric nanoparticles. Int J Pharm. 2006; 307(1):93–102. [PubMed: 16303268]
- 31. Malugin A, Ghandehari H. Cellular uptake and toxicity of gold nanoparticles in prostate cancer cells: a comparative study of rods and spheres. J Appl Toxicol. 2010; 30(3):212–217. [PubMed: 19902477]
- 32. Fischer HC, Liu LC, Pang KS, Chan WC. Pharmacokinetics of nanoscale quantum dots: *In vivo* distribution, sequestration, and clearance in the rat. Adv Funct Mater. 2006; 16(10):1299–1305.
- 33. Sadauskas E, Wallin H, Stoltenberg M, et al. Kupffer cells are central in the removal of nanoparticles from the organism. Part Fibre Toxicol. 2007; 4:10. [PubMed: 17949501]
- 34. Bohnsack JF, Brown EJ. The role of the spleen in resistance to infection. Annu Rev Med. 1986; 37:49–59. [PubMed: 3518612]
- 35. Cho NH, Cheong TC, Min JH, et al. A multifunctional core-shell nanoparticle for dendritic cell-based cancer immunotherapy. Nat Nanotechnol. 2011; 6(10):675–682. [PubMed: 21909083]
- 36. Manolova V, Flace A, Bauer M, Schwarz K, Saudan P, Bachmann MF. Nanoparticles target distinct dendritic cell populations according to their size. Eur J Immunol. 2008; 38(5):1404–1413. [PubMed: 18389478]
- 37. Dinauer N, Balthasar S, Weber C, Kreuter J, Langer K, Von Briesen H. Selective targeting of antibody-conjugated nanoparticles to leukemic cells and primary T-lymphocytes. Biomaterials. 2005; 26(29):5898–5906. [PubMed: 15949555]
- 38. Richter K, Agnellini P, Oxenius A. On the role of the inhibitory receptor LAG-3 in acute and chronic LCMV infection. Int Immunol. 2010; 22(1):13–23. [PubMed: 19880580]
- 39. Murakami T, Chen X, Hase K, Sakamoto A, Nishigaki C, Ohno H. Splenic CD19<sup>-</sup> CD35<sup>+</sup>B220<sup>+</sup> cells function as an inducer of follicular dendritic cell network formation. Blood. 2007; 110(4): 1215–1224. [PubMed: 17519390]
- 40. Goldberg MV, Drake CG. LAG-3 in cancer Immunotherapy. Curr Top Microbiol Immunol. 2011; 344:269–278. [PubMed: 21086108]
- 41. Steinmetz NF, Ablack AL, Hickey JL, et al. Intravital imaging of human prostate cancer using viral nanoparticles targeted to gastrin-releasing peptide receptors. Small. 2011; 7(12):1664–1672. [PubMed: 21520408]
- 42. Steinmetz NF, Mertens ME, Taurog RE, et al. Potato virus X as a novel platform for potential biomedical applications. Nano Lett. 2010; 10(1):305–312. [PubMed: 20017489]
- 43. Christian DA, Cai S, Garbuzenko OB, et al. Flexible filaments for *in vivo* imaging and delivery: persistent circulation of filomicelles opens the dosage window for sustained tumor shrinkage. Mol Pharm. 2009; 6(5):1343–1352. Demonstrates shape-derived advantages of filamentous particles; prolonged circulation half-life resulting in sustained therapeutic effects is reported using filomicelles loaded with chemotherapeutic drugs. [PubMed: 19249859]
- 44. Moghimi SM, Hunter AC, Andresen TL. Factors controlling nanoparticle pharmacokinetics: an integrated analysis and perspective. Annu Rev Pharmacol Toxicol. 2012; 52:481–503. [PubMed: 22035254]
- 45. Toraya-Brown S, Sheen MR, Baird JR, et al. Phagocytes mediate targeting of iron oxide nanoparticles to tumors for cancer therapy. Integr Biol (Camb ). 2012; 5(1):159–171. [PubMed: 22935885]
- 46. Li M, Al-Jamal KT, Kostarelos K, Reineke J. Physiologically based pharmacokinetic modeling of nanoparticles. ACS Nano. 2010; 4(11):6303–6317. [PubMed: 20945925]
- 47. Torosean S, Flynn B, Axelsson J, et al. Nanoparticle uptake in tumors is mediated by the interplay of vascular and collagen density with interstitial pressure. Nanomedicine. 2012; 9(2):151–158. Provides crucial insight into the role of physiological factors, such as tumor stroma density and interstitial pressure, in influencing the ability of nanoparticles to localize in the tumor, thereby influencing their therapeutic effeciency. [PubMed: 22841910]
- 48. Lico C, Mancini C, Italiani P, et al. Plant-produced potato virus X chimeric particles displaying an influenza virus-derived peptide activate specific CD8<sup>+</sup> T cells in mice. Vaccine. 2009; 27(37): 5069–5076. [PubMed: 19563889]

49. Steinmetz NF, Manchester M. PEGylated viral nanoparticles for biomedicine: the impact of PEG chain length on VNP cell interactions *in vitro* and *ex vivo*. Biomacromolecules. 2009; 10(4):784–792. [PubMed: 19281149]

- Raja KS, Wang Q, Gonzalez MJ, Manchester M, Johnson JE, Finn MG. Hybrid virus-polymer materials.
   Synthesis and properties of PEG-decorated cowpea mosaic virus. Biomacromolecules.
   2003; 4(3):472–476. [PubMed: 12741758]
- 51. Perry JL, Reuter KG, Kai MP, et al. PEGylated PRINT nanoparticles: the impact of PEG density on protein binding, macrophage association, biodistribution, and pharmacokinetics. Nano Lett. 2012; 12(10):5304–5310. [PubMed: 22920324]
- 52. Svergun DI, Ekstrom F, Vandegriff KD, et al. Solution structure of poly(ethylene) glycol-conjugated hemoglobin revealed by small-angle X-ray scattering: implications for a new oxygen therapeutic. Biophys J. 2008; 94(1):173–181. [PubMed: 17827244]
- 53. Degennes PG. Polymers at an interface a simplified view. Adv Colloid Interfac. 1987; 27(3–4): 189–209.

#### **Executive summary**

• Equal densities of PEG5000 and A647 fluorophore were bioconjugated to potato virus X (PVX; i.e., ~380 molecules of each), which equates to 30% of the coat proteins modified with polyethylene glycol (PEG) and an additional 30% of the coat proteins modified with A647.

- PVX is cleared from circulation by the mononuclear phagocyte system and
  accumulates in the spleen and liver; the majority of PVX filaments are cleared
  via the hepatobiliary route, while a smaller amount is processed through renal
  clearance.
- Immunofluorescence imaging indicates that PVX is taken up by resident macrophages (e.g., Kupffer cells) in the liver.
- In the spleen, PVX is localized in the B-cell follicle-rich white pulp and promotes a significant increase in CD223<sup>+</sup> T cells at 72 h postadministration, reflecting the immunogenic properties of PVX.
- Data indicate that PEGylation, with approximately 380 copies of PEG5000, is insufficient to avoid uptake in antigen-presenting cells.
- Up to 30% of the injected PVX dose is retained in tumor tissue for several days.
- PVX demonstrates tumor homing in several different tumor xenograft mouse models, including colon cancer, brain cancer and breast cancer models.
- Gradual build-up of PVX in tumors days past its circulation half-life suggests a secondary mechanism of tumor homing (in addition or instead of enhanced permeability and retention effect).

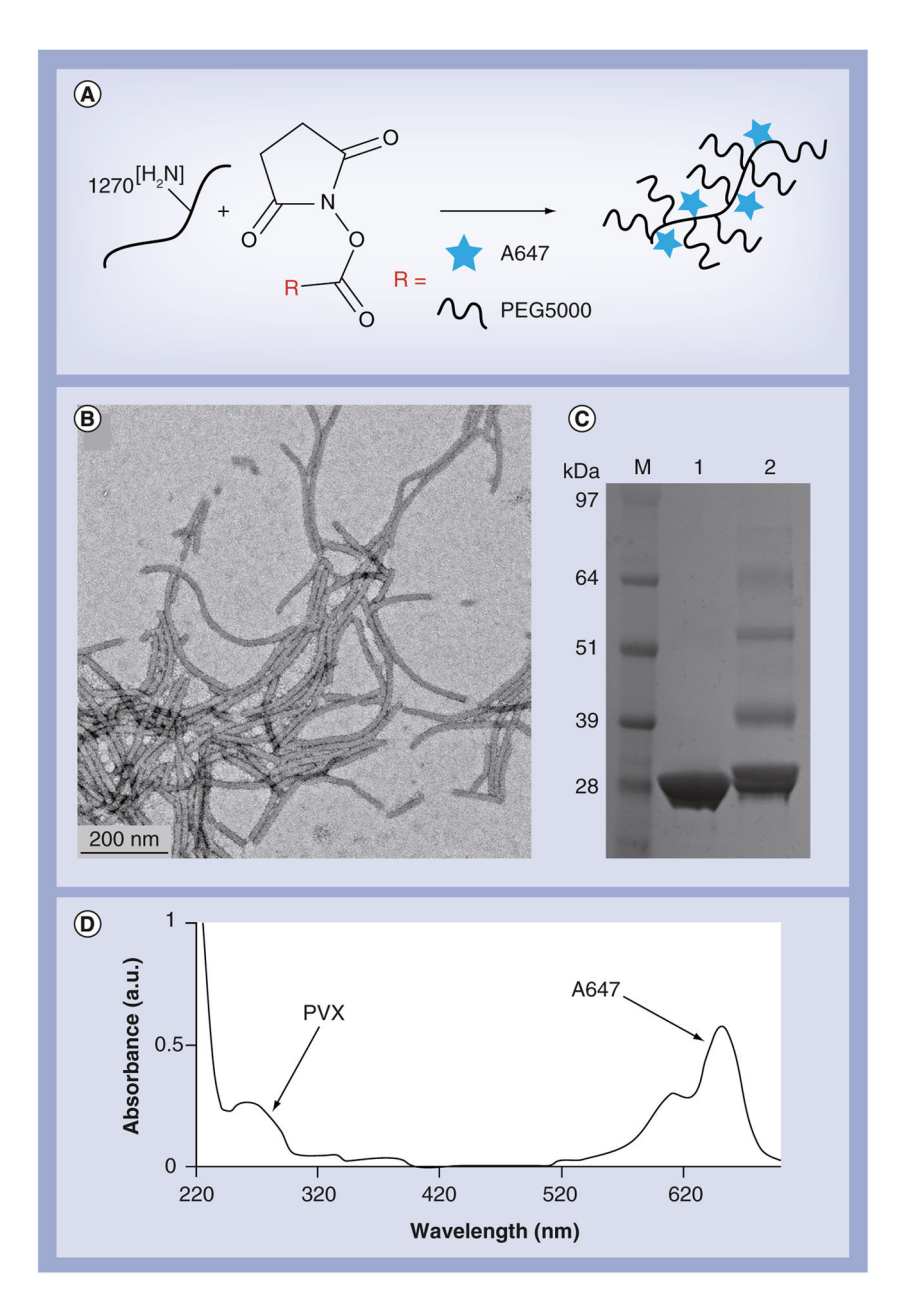


Figure 1. Characterization of A647-PVX-PEG

(A) Scheme of PVX labeling using N-hydroxysuccinimide-activated esters of A647 dye and PEG5000 at solvent-exposed lysine side chains; (B) transmission electron microscopy image of negatively stained A647-PVX-PEG; (C) SDS gel comparing native PVX (lane 1) with modified A647-PVX-PEG (lane 2); band-profile analysis indicates that 30% of the coat proteins were labeled with PEG (i.e., ~380 PEGs per PVX); (D) UV/visible spectrum of A647-PVX-PEG: the ratio of A647 and PVX protein concentration indicates labeling with approximately 380 A647 dyes per PVX.

PEG: Polyethylene glycol with a molecular weight of 5000 Da; PVX: Potato virus X.

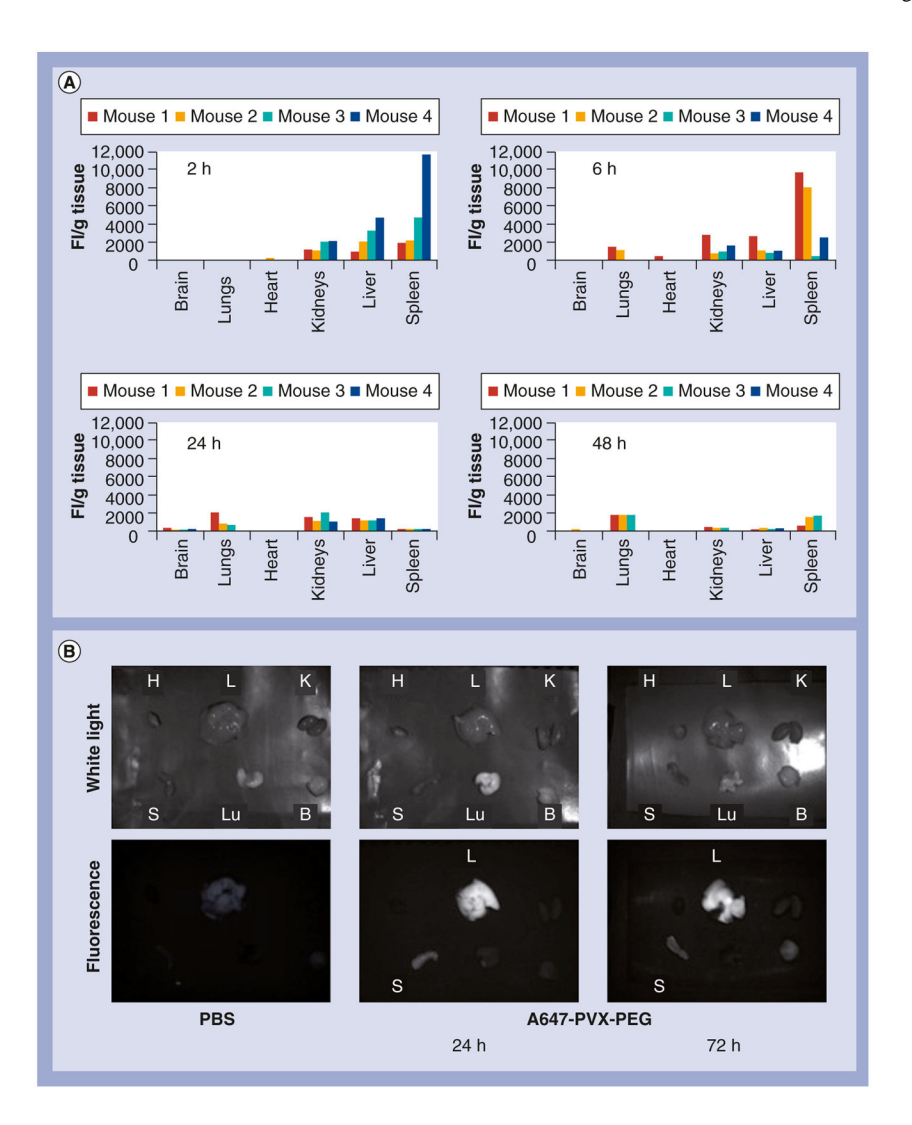


Figure 2. Biodistribution of A647-PVX-PEG in Balb/c mice

- (A) Fluorescence intensity (of A647-PVX-PEG) per gram tissue weights (FI/g) at 2, 6, 24 and 48 h postadministration of A647-PVX-PEG (intravenously via tail vein of Balb/c animals) measured based on fluorescence intensity; (B) *ex vivo* imaging, using the Maestro<sup>™</sup> Imaging System (Perkin Elmer, MA, USA), of tissues harvested from Balb/c mice injected with PBS (at 24 h) and A647-PVX-PEG (at 24 and 72 h) postadministration.
- B: Brain; FI: Fluorescence intensity; K: Kidney; H: Heart; L: Liver; Lu: Lungs; PBS: Phosphate-buffered saline; PEG: Polyethylene glycol; PVX: Potato virus X; S: Spleen.

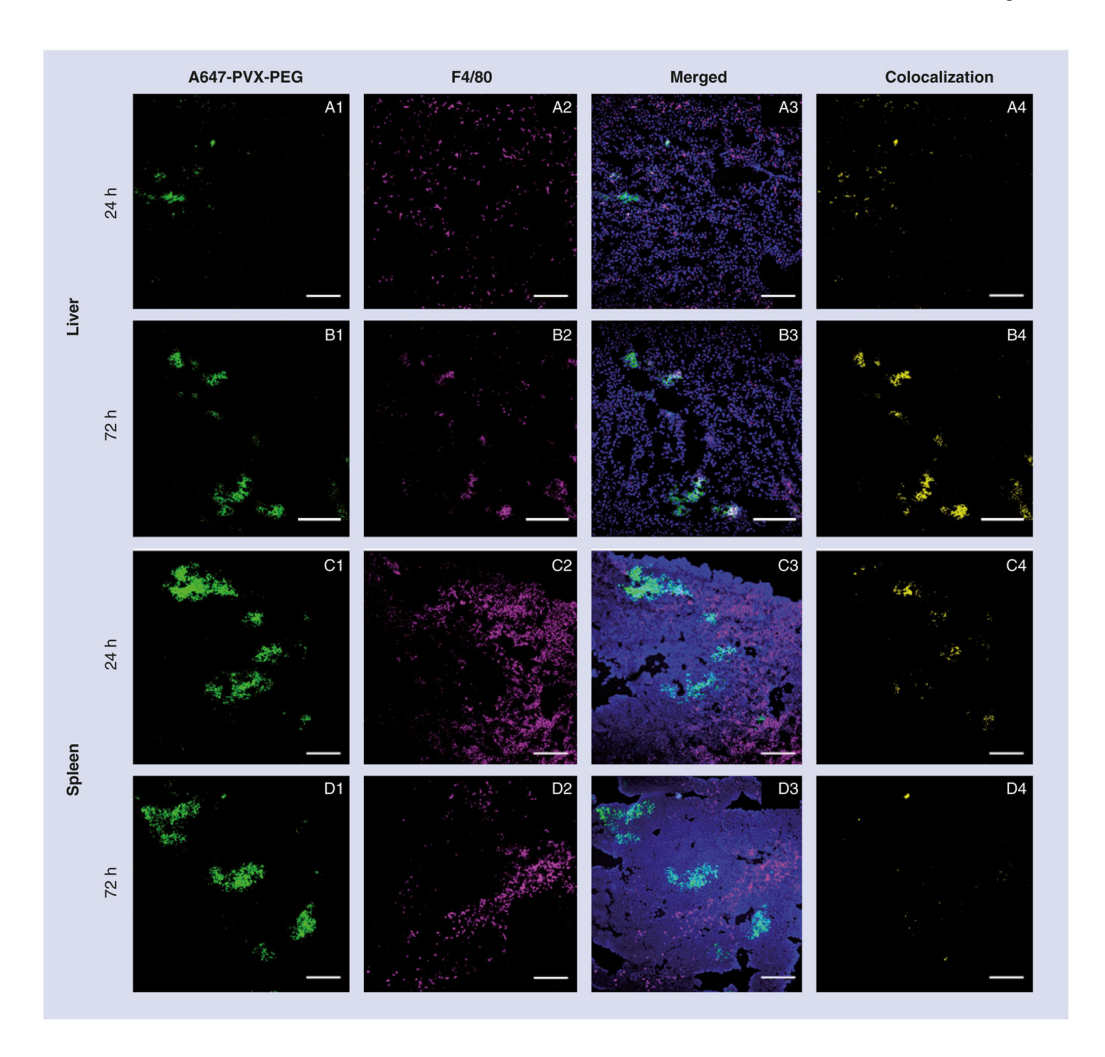


Figure 3. Immunofluorescence imaging of liver and spleen after potato virus X administration Liver and spleen sections from Balb/c mice after intravenous administration of A647-PVX-PEG (green) into the tail vein stained for macrophage marker F4/80. (A & B) show the liver 24 and 72 h postadministration, respectively; (C & D) shows the spleen 24 and 72 h postadministration, respectively; magenta). (A4, B4, C4 & D4) shows the corresponding colocalization of PVX with F4/80 marker (yellow). Scale bars represent 200 μm. PEG: Polyethylene glycol; PVX: Potato virus X.

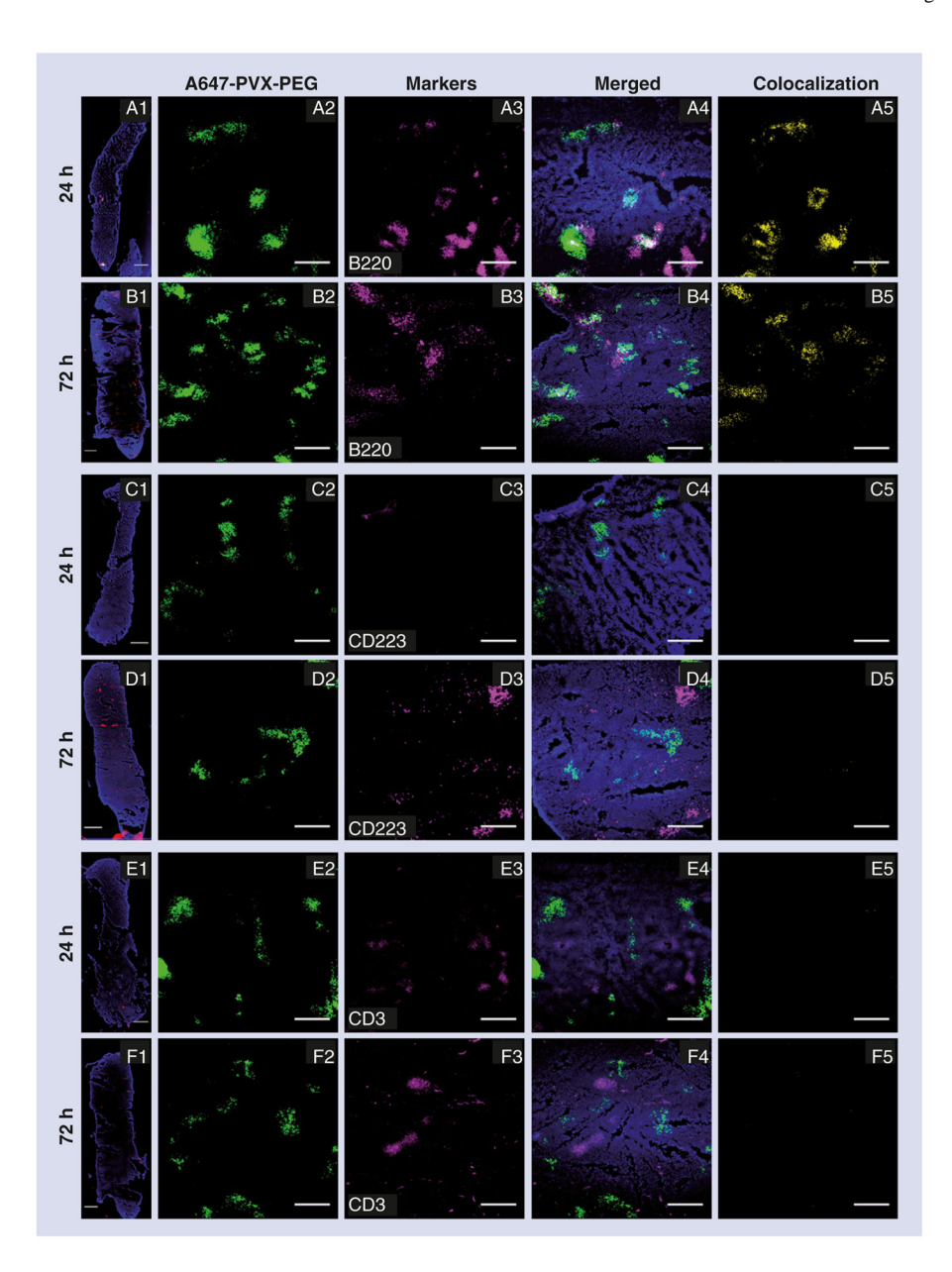


Figure 4. Immunofluorescence imaging of the spleen after potato virus  $\boldsymbol{X}$  administration and colocalization with cellular markers

Immunohistological analysis of spleen sections 24 and 72 h postintravenous administration of A647-PVX-PEG in Balb/c mice. (A1 & B1) are the fluorescence microscopic image of whole spleen section stained for PVX (green), B220 marker (magenta) and nuclei (4′,6-diamidino-2-phenylindole) after 24 and 72 h, respectively; (A2–A4 & B2–B4) are the corresponding confocal images from the regions of the same spleen. (C1 & D1) are the spleens similarly stained for CD223 (magenta) at 24 and 72 h (C2–C4 & D2–D4) with corresponding confocal images. (E1 & F1) are the spleens stained for CD3 (magenta), (E2–E4 & F2–F4) are the corresponding confocal images. Colocalization analysis was carried out using ImageJ software and is shown in yellow; M2 coefficients are reported in Table 1. Scale bars are 1000 μm for (A1–F1) and 50 μm for all confocal images.

PEG: Polyethylene glycol; PVX: Potato virus X.

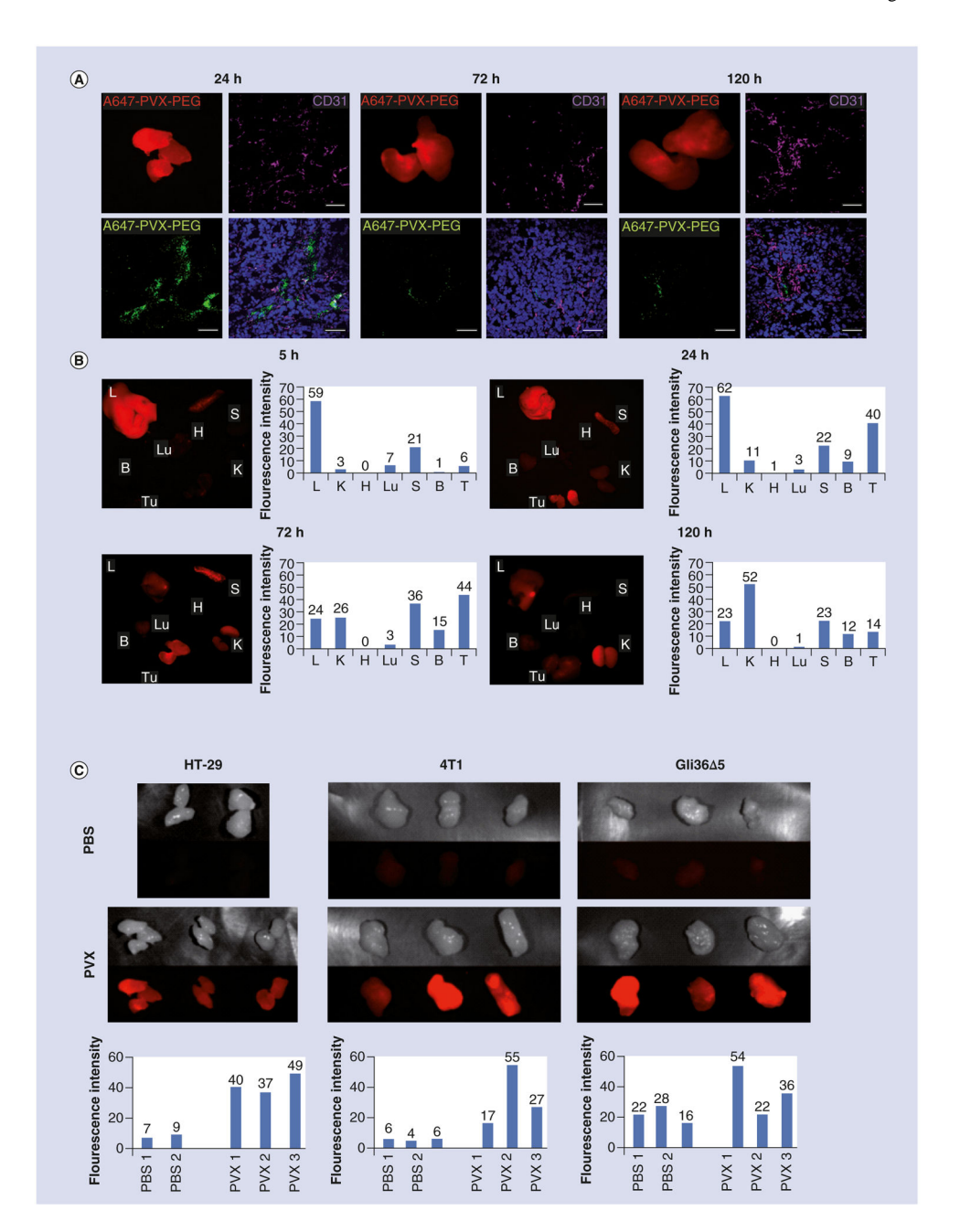


Figure 5. Tumor homing and biodistribution of potato virus X (facing page)

Maestro<sup>™</sup> Imaging System (Perkin Elmer, MA, USA) analysis of HT-29, 4T1 and Gli36 5

tumor xenografts from animals sacrificed at different time points postintravenous

tumor xenografts from animals sacrificed at different time points postintravenous administration of A647-PVX-PEG. (A) Maestro images of HT-29 tumors at 24, 72 and 120 h postadministration and the confocal images of corresponding tumor sections showing PVX (green) penetration into tumor tissue via the tumor vasculature CD31 (red; scale bar represents 50  $\mu$ m). (B) Representative Maestro images of tissue biodistribution in the HT-29 xenograft mice (n = 3) at various time points postinjection and the corresponding relative fluorescence signal intensity measured using ImageJ. (C) Comparative Maestro Imaging System analysis of HT-29, 4T1 and Gli36 5 tumor xenografts 24 h postinjection with

phosphate-buffered saline or A647-PVX-PEG and their corresponding fluorescence intensities analyzed using ImageJ (NIH, MD, USA) software (n=3, except for HT-29 tumors/PBSwith n=2, one animal had to be sacrificed).

B: Brain; H: Heart; K: Kidney; L: Liver; Lu: Lung; PBS: Phosphate-buffered saline; PEG: Polyethylene glycol; PVX: Potato virus X; S: Spleen; Tu: Tumor.

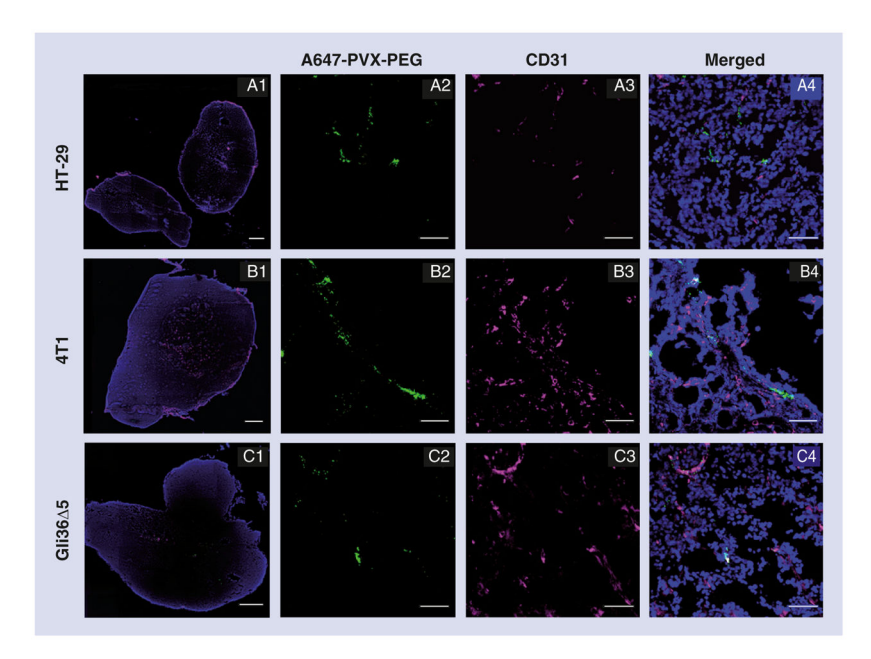


Figure 6. Immunofluorescence imaging of tumors

Fluorescence microscopic analysis of whole tumor tissues (**A1, B1 & C1**) and confocal microscopic analysis of cryosections of PVX (green)-injected HT29, 4T1 and Gli36 5 tumors 24 h postadministration. Tumor sections were stained for endothelial cell marker CD31 (magenta) and 4',6-diamidino-2-phenylindole (blue). Scale bars represent 1000  $\mu$ m for (**A1, B1 & C1**) and 50  $\mu$ m for (**A2–A4, B2–B4 & C2–C4**).

PEG: Polyethylene glycol; PVX: Potato virus X.

Table 1

Colocalization of A647-potato virus X-polyethylene glycol with biomarkers in the liver, spleen and tumors.

Location	Biomarker	Mander's coefficients	
		24 h	72 h
Liver	F4/80	0.351	0.913
	CD31	0.976	0.379
Spleen	F4/80	0.152	0.023
	CD31	0.053	0.044
	B220	0.866	0.762
	CD223	0.007	0.059
	CD3	0.006	0.021
	CD21/35	0.964	0.098
HT29 tumors	CD31	0.54	0.068
	B220	0.465	-
	F4/80	0.345	-
4T1 tumors	CD31	0.367	-
	B220	0.574	-
	F4/80	0.324	-
Gli36 5 tumors	CD31	0.855	-
	B220	0.108	_
	F4/80	0.264	=